INL/JOU-20-57656-Revision-0

Microstructure and diffusion behavior of uranium fuel with minor additives

July 2020

Yi Xie, Michael T Benson

Changing the World's Energy Future

Idaho National Laboratory

INL is a U.S. Department of Energy National Laboratory operated by Battelle Energy Alliance, LLC

INL/JOU-20-57656-Revision-0

Microstructure and diffusion behavior of uranium fuel with minor additives

Yi Xie, Michael T Benson

July 2020

Idaho National Laboratory
Idaho Falls, Idaho 83415

http://www.inl.gov

Prepared for the
U.S. Department of Energy
Under DOE Idaho Operations Office
Contract DE-AC07-05ID14517, DE-AC07-05ID14517

Microstructure and diffusion behavior of uranium fuel with minor additives

Yi Xie, Michael T. Benson

Idaho National Laboratory, P.O. Box 1625, MS 6188, Idaho Falls, ID 83415

Corresponding Author Information

Michael T. Benson, phone: (208) 533-8870, FAX: (208) 533-7863, email: michael.benson@inl.gov.

Abstract

Fission product lanthanides in metallic fuels are known to cause adverse fuel-cladding chemical interaction (FCCI). Tin (Sn) and palladium (Pd) are being explored as the potential additives to reduce or mitigate lanthanide-induced FCCI by forming stable Sn-Ln and Pd-Ln compounds. The current study is an investigation of the fuel alloys, U-4Sn, U-4Sn-4Ln, U-4Pd, and U-4Pd-4Ln (wt. %), and their diffusion behaviors with Fe. Microstructural analysis was performed using scanning electron microscopy (SEM). The binary phases in the UPd and USn alloys are identified as UPd_3 and suspected U_2Sn, where U_2Sn is unknown in the literature. The binary phases in the UPdLn alloy are identified as PdLn and Pd-rich Pd-Ln (Pd_4Ln_3 and Pd_3Ln_2), and in the USnLn alloy is SnLn. Diffusion of Fe with these binary phases is insignificant compared to the diffusion with U. The Ln-induced FCCI can be mitigated by the additives.

Keywords: Metallic fuel; FCCI; Fuel additive

1. Introduction

The metallic fuels U-Zr and U-Pu-Zr performed well under irradiation during the Experimental Breeder Reactor II (EBR-II) [1] and Fast Flux Test Facility (FFTF) [2] programs, and they have promising application due to the high thermal conductivity, potential high burn-up, and inherent recyclability [3][4]. A notable fuel application issue is fuel-cladding chemical interaction (FCCI), primarily induced by fission product lanthanides that migrate to the fuel periphery and react with the cladding [5].

An additive approach that would bind free lanthanides by forming stable compounds has been investigated, with two promising candidates being Sn [6][7][8] and Pd [9][10][11][12][13][14]. These additives are also fission products, naturally generated by irradiation [15], though they are produced in small amounts and therefore have to be artificially supplemented. Accordingly, the additive approach is to add enough elements to bind lanthanides produced for some initial burnup, and hence to extend fuel lifetime.

During irradiation, the fission products, including lanthanides, noble gases, and alkali metals are generated. The existing U-Zr and U-Pu-Zr fuel pin systems are complicated due to multiple fuel constituents and fission products, and using an additive in the fuel further complicates this system. Characterizing the phases present and chemical interactions (in the fuel and with cladding, i.e. FCCI) out-of-pile is the first step towards understanding the fuel's behavior during irradiation.

To this end, the out-of-pile microstructure and FCCI have been investigated for the U-Sn/Pd and U-Sn/Pd-Ln systems. Specific compositions of the alloys are listed in Table 1. The four most prevalent lanthanides (Nd, Ce, Pr, La), as determined for an EBR-II irradiated U-10Zr fuel pin [14], are used to represent the lanthanides present during irradiation. Both the as-cast (as the alloy would be when first inserted into a reactor) and annealed microstructures are presented. Interactions with Fe have been investigated for each alloy using diffusion couples. Scanning electron microscopy (SEM) was used to characterize the microstructure for both the alloys and the diffusion couples.

Table 1. Alloy compositions.

Alloy	wt. %	at. %
UPd	96U-4Pd	91.5U-8.5Pd
UPdLn*	92U-4Pd-4Ln	85.5U-8.3Pd-6.2Ln
USn	96U-4Sn	92.3U-7.7Sn
USnLn*	92U-4Sn-4Ln	86.3U-7.5Sn-6.2Ln

* Ln = 53Nd-25Ce-16Pr-6La wt. % (52.3Nd-25.4Ce-16.2Pr-6.1La at. %)

2. Experiment

Table 1 provides the compositions of the four alloys prepared. The alloys contain Sn/Pd without lanthanides are intended to exhibit the behavior of fresh fuel prior to irradiation. The Ln is a mix of four most prevalent lanthanide fission products found in an EBR-II U-10Zr fuel pin [14], Nd, Ce, Pr, and La, with a composition of 53Nd-25Ce-16Pr-6La wt. %. The lanthanides content corresponds to approximately 20 % burnup. All materials except U were obtained from Alfa Aesar and used as received. The lanthanides were obtained as rods, packaged in mylar under argon.

All casting operations were carried out in an arc-melter, with a tungsten electrode, within an argon atmosphere glovebox with high purity argon as a cover gas. After adding each element, the resulting cast button was flipped and re-melted three times to ensure homogeneity. To prepare USn and UPd alloys, the appropriate amounts of U and Sn or Pd were arc-melted together. Sn and U have significantly different melting points (1135 °C for U and 232 °C for Sn), with the melting point of Sn being very low. This does not present any difficulties when arc melting these elements, though, since the boiling point for Sn is high, and the vapor pressure is low. To prepare USnLn and UPdLn alloys, pre-alloy buttons of U-Sn and U-Pd were prepared, followed by the addition of Ln mix. The Ln mix was prepared by arc melting the appropriate amount of each lanthanide together in one step. The buttons were cast into 5-mm diameter pins.

Approximately 3 mm from each pin was cut for annealing. The samples were wrapped in tantalum (Ta) foil, then sealed in quartz tubes under vacuum. The quartz tube was placed in a furnace at 873 K for 504 hours, based on a typical fuel-cladding interface temperature. After the heat treatment, the samples were quenched in water. The samples were then cut to expose a fresh surface for analysis.

Approximately 3 mm from each pin was cut for the diffusion couple. To prepare samples for diffusion couple, the surface was ground flat using SiC grinding paper, followed by polishing with 9 μm, 3 μm, and 1 μm polycrystalline diamond suspensions. The initial polishing steps

were performed in air, while the 3 μm and 1 μm steps were performed in an argon glovebox. Approximately 3 mm of a 5 mm Fe rod, with purity of 99.995 % obtained from Alfa Aesar, was prepared in the same manner. The samples were then placed together with polished surfaces in contact and surrounded by Ta foil, in a Kovar alloy diffusion couple jig. The jigs were sealed in quartz tubes under vacuum. The diffusion couples were heated at 873 K for 504 hours. After the heat treatment, the diffusion couples were quenched in water and removed from the jig for analysis.

Scanning electron microscopy (SEM) was performed on the as-cast, annealed and diffusion couple samples. The samples were mounted in a 31.8 mm diameter phenolic metallographic mount filled with epoxy. Samples were polished by grinding surfaces flat with SiC grinding paper followed by polishing with polycrystalline diamond suspensions, starting with 9 μm, then 3 μm, and finally 1 μm. The polished samples were analyzed with a sputtered coating of approximately 10 nm gold or 15 nm carbon to minimize charging of the metallographic mount.

A JEOL JSM-IT500HR SEM equipped with an Oxford Instruments X-Max 20 silicon drift energy dispersive X-ray spectrometer (EDS) was used for analysis. The EDS is controlled by Oxford AZtec software, which also provides image acquisition capabilities. The SEM was operated at an accelerating voltage of 20 keV and a nominal beam current of approximately 14 nA (which can vary somewhat with column conditions) for these analyses. All the X-ray spectra were accumulated for 45 live seconds. Spectra were collected over an energy range of 0 – 20 keV, which covers characteristic X-ray energies from all analytes. Spectra were quantified using so-called “standardless” analysis, which uses a stored library of reference spectra to quantify unknown spectra rather than physical standards. This method is generally accurate to a few at./at. % range, depending on sample and microscope (observation) conditions.

3. Results

3.1. UPd

3.1.1. Alloy microstructure

The microstructure and elemental distribution of as-cast UPd alloy is shown in Figure 1, with EDS data listed in *Table 2*. The microstructure contains light grey, dark grey, and black regions. The composition of grey regions is 95-97 at. % U and 3-5 at. % Pd, with no significant difference in the compositions between the light and dark grey regions. The intergranular region is black, and is rich in Pd, as shown in the EDS maps in Figure 1c. EDS maps are used to indicate the composition of the intergranular region. Due to the small size, quantitative EDS is not possible with SEM due to the large interaction volume. U-oxide precipitates were observed, indicated by red arrows in Figure 1b, and indicated by the EDS mapping of O shown in Figure 1c.

After annealing, the microstructure is similar, shown in Figure 2, with EDS data provided in *Table 2*. The light and dark grey phases are spinodal-like and coexisting in the grain. The EDS data, boxes 1 and 2 in Figure 2b and *Table 2*, indicate compositions of these phases are the same as in the as-cast. In addition, the black phase at grain interface is thicker and less continuous. Being slightly larger intergranular deposits than in the as-cast sample, quantitative EDS analysis was performed, indicating this phase contains 26 at. % U and 74 at. % Pd (points 3 and 4), which is the composition of the known phase UPd_3, based on the U-Pd binary phase diagram [16]. The composition of the UPd alloy (91.5U-8.5Pd at. %) is located between UPd_3 and α-U, based on

the phase diagram. Therefore, it is reasonable that UPd_3 and U are the phases present.

Nanometer-sized Pd-precipitates, i.e., grey precipitates in the grains as shown in Figure 1b and Figure 2b, are dispersed in the UPd alloy matrix. They are transformed from the solid solute Pd in U when the alloy is cooled from elevated temperatures after melting. The solid solubility of Pd in U is up to 5 at. % at elevated temperature, and almost 0 at. % at room temperature, based on the U-Pd binary phase diagram [16]. The EDS date, listed in Table 2, support that the alloy matrix contains roughly 5 at. % Pd, which is in accordance with the solid solubility of Pd in U at elevated temperature.

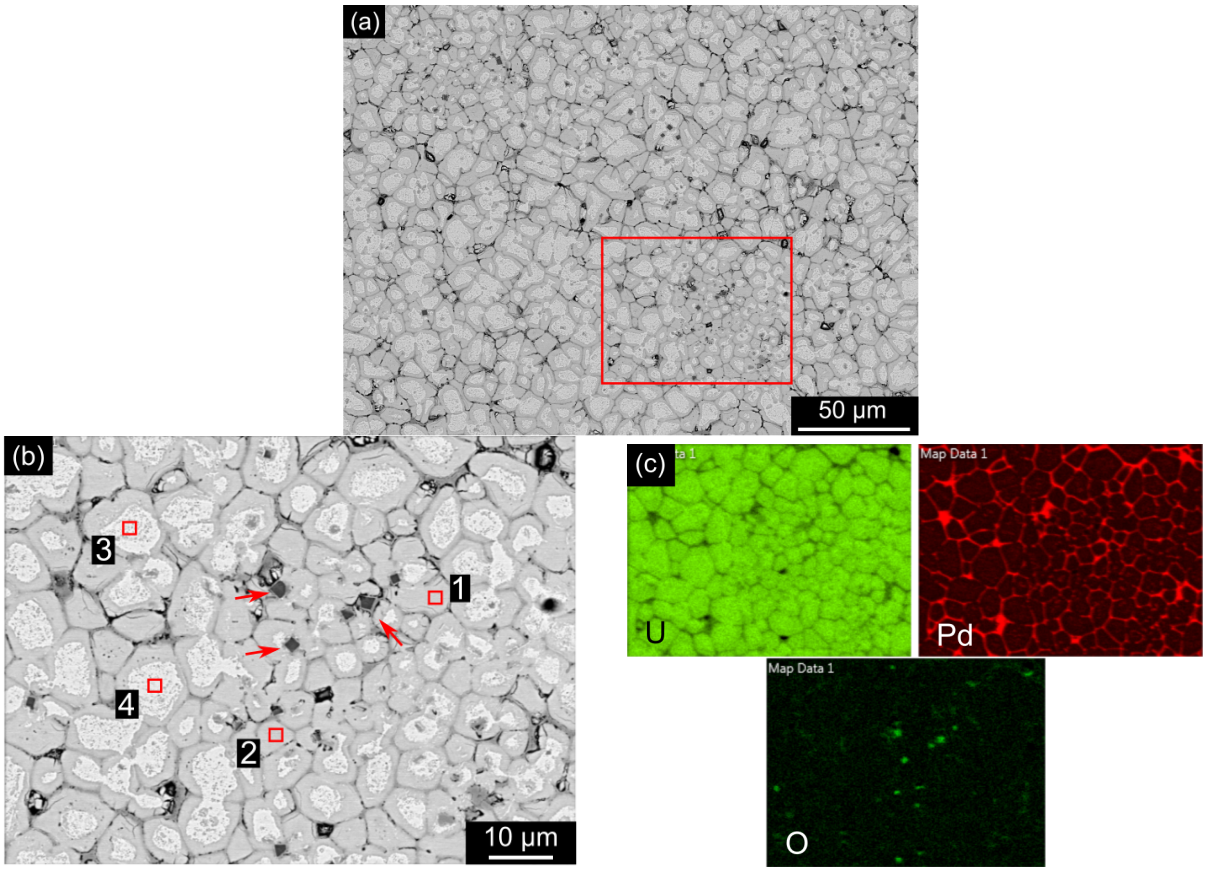

Figure 1. SEM backscattered electron (BSE) images of as-cast UPd. The red rectangle in Figure 1a indicates the location of the magnified image shown in Figure 1b. The red arrows in Figure 1b indicate U-oxide. EDS maps of U, Pd, and O for Figure 1b are shown in Figure 1c. Corresponding EDS data are listed in Table 2.

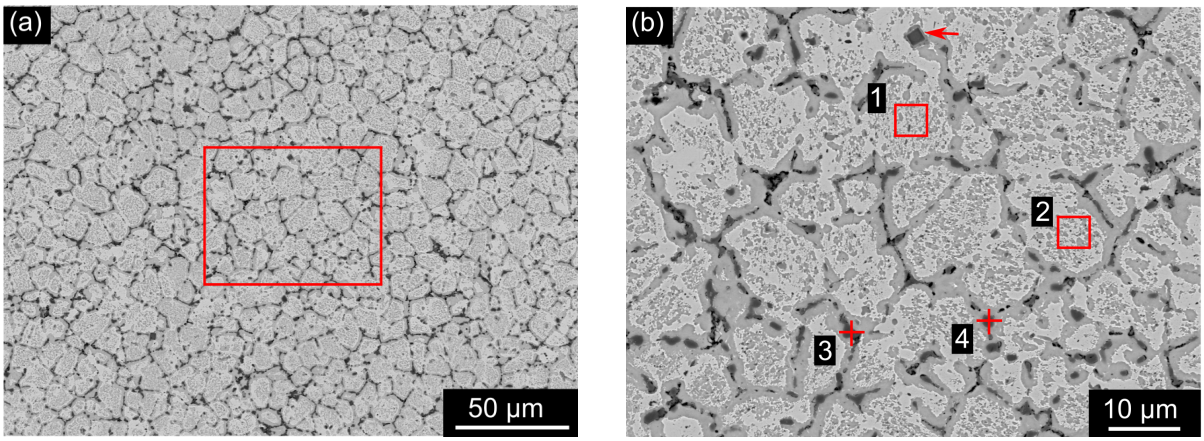

Figure 2. SEM BSE images of annealed UPd. The red rectangle in Figure 2a indicates the location of the magnified image shown in Figure 2b. The red arrow in Figure 2b indicates U-oxide. Corresponding EDS data are provided in Table 2.

Table 2. EDS data for the points and boxes shown in Figure 1b and Figure 2b. Values in at. %.

	U	Pd	Phase[a]
	*Figure 1*b		
1	97	3	α-U
2	96	4	α-U
3	95	5	α-U
4	95	5	α-U
	*Figure 2*b		
1	95	5	α-U
2	95	5	α-U
3	26	75	UPd_3
4	26	74	UPd_3

[a] Suggested phase based on the SEM EDS analysis.

3.1.2. Diffusion between UPd and Fe

The diffusion interface between the UPd alloy and Fe is shown in Figure 3, with EDS data provided in Table 3. The EDS line spectrum, indicated by the red arrow in Figure 3a, shown in Figure 3c, indicates the Fe diffusion roughly 20 µm into the UPd alloy, forming a dark grey layer (at a distance of 30-50 µm). The Fe content in the diffusion layer decreases with the diffusion depth. Nevertheless, diffusion from the UPd alloy into Fe was not observed. The interface between UPd and Fe, shown in Figure 3a and 3b, is flat and straight, which indicates the original contact surface. On the Fe side, there is no U or Pd observed, so UPd alloy did not diffuse toward Fe.

Small, nanometer-sized precipitates are observed in the UPd side of the diffusion couple, around the intergranular boundaries. There are several peaks around 35 µm in the line scan indicating an increase in Pd and a decrease in U. As Fe diffuses into the U matrix, Pd is coming out of the intergranular boundaries and reacting with Fe. The size of these particles prevents quantitative EDS analysis to determine composition, though. The line scan, shown in Figure 3c,

indicates the particles are Fe-rich, although that doesn't match known Pd-Fe intermetallics based on the Pd-Fe phase diagram [17]. Identifying equilibrium structures in the diffusion zone is not always possible, though, since the diffusion zone is not in equilibrium.

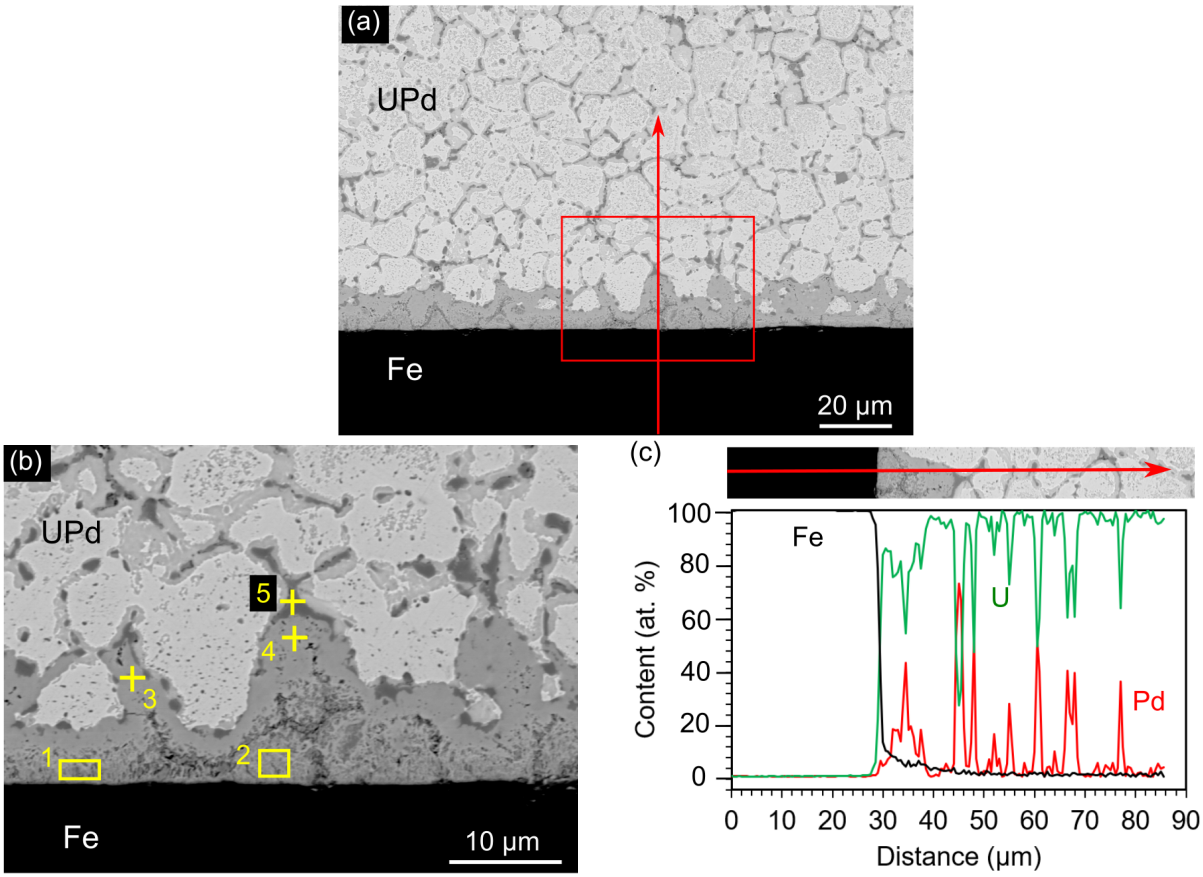

Figure 3. (a) SEM BSE image of the UPd/Fe interface. The box indicates the magnified image present in Figure 3b. The red arrow in Figure 3a indicates the EDS line spectrum, shown in Figure 3c. The EDS point data are provided in Table 3.

Table 3. SEM EDS data for the points and boxes in Figure 3b. Values in at. %.

	U	Pd	Fe	Phase[a]
1	85	5	9	α-U
2	89	3	9	α-U
3	96	1	3	α-U
4	97	1	3	α-U
5	25	74	2	UPd_3

[a] Suggested phase based on the SEM EDS analysis.

3.2. UPdLn

3.2.1. Alloy microstructure

The microstructure of as-cast UPdLn alloy is shown in Figure 4, with corresponding EDS data listed in Table 4. A large precipitate was observed in the alloy, comprised of 50 at. % Pd and 50 at. % Ln (points 1-3 in Figure 4b and Table 4), which is a ratio of the known 1:1 PdLn binary phase in the Pd-Ln system. Other, smaller precipitates contain 50 at. % Pd, 43 at. % Ln, and 7 at. % U (points 7-8). There is a slight excess of Pd over Ln in the alloy, so these small precipitates are tentatively identified as Pd_4Ln_3 with solid solubility for U. It is also possible that the small precipitates are PdLn, but the EDS values might be affected by the beam interaction volume. The fuel matrix contains 97 at. % U and 3 at. % Pd (box 4), as was observed for the UPd alloy. Some grey precipitates are randomly dispersed in the matrix (points 5-6) that have the same composition as the matrix. The reason for the slighter darker contrast in these is not known. If it's impurities, oxygen, or some other reason, it is below the detection limits of the SEM.

The microstructure of annealed UPdLn alloy is shown in Figure 5, with EDS data provided in Table 5. The larger precipitate in Figure 5b has two different contrast regions. The prominent, darker region is Pd-rich, with some lanthanides present, while the lighter region matched the smaller precipitates scattered throughout the microstructure, with a composition of ~57Pd-37Ln-6U at.% that roughly corresponds to Pd_3Ln_2 (57Pd:37Ln) with U from the surrounding matrix contributed to the X-ray counts, or Pd_4Ln_3 with solid solubility for U (approximately 6 at.%), although this is uncertain. The Pd_3Ln_2 type phase does not exist in the phase diagram, but a previous transmission electron microscope (TEM) study has observed the composition with a diffraction pattern that could not be indexed [13]. The fuel matrix has light grey and grey regions with the same compositions, 99 at. % U and 1 at. % Pd (points 8-10), as was also observed in UPd, although the Pd content is lower. The Pd-Ln precipitates apparently consumed some of the Pd located in the matrix. The darker grey regions may contain more Pd, causing the contrast difference. If so, the EDS analysis is not able to differentiate the Pd content.

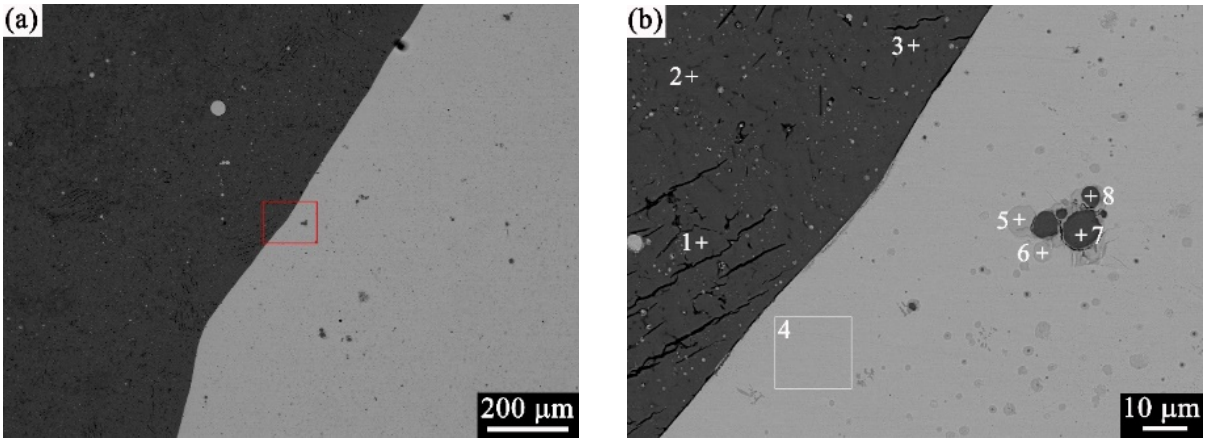

Figure 4. SEM BSE images of as-cast UPdLn. The red rectangle in Figure 4a indicates the location of the magnified image shown in Figure 4b. Corresponding EDS data are listed in Table 4.

Table 4. EDS data for the points and boxes shown in Figure 4b. Values in at. %.

	U	Pd	Nd	Ce	Pr	La	Phase[a]
1	2	50	25	12	8	3	PdLn
2	2	49	26	12	8	3	PdLn
3	2	50	25	12	8	3	PdLn

4	97	3	0	0	0	0	α-U
5	98	2	0	0	0	0	α-U
6	98	2	0	0	0	0	α-U
7	7	50	18	17	7	1	Pd_4Ln_3/PdLn
8	8	51	17	17	6	1	Pd_4Ln_3/PdLn

[a] Suggested phase based on the SEM EDS analysis.

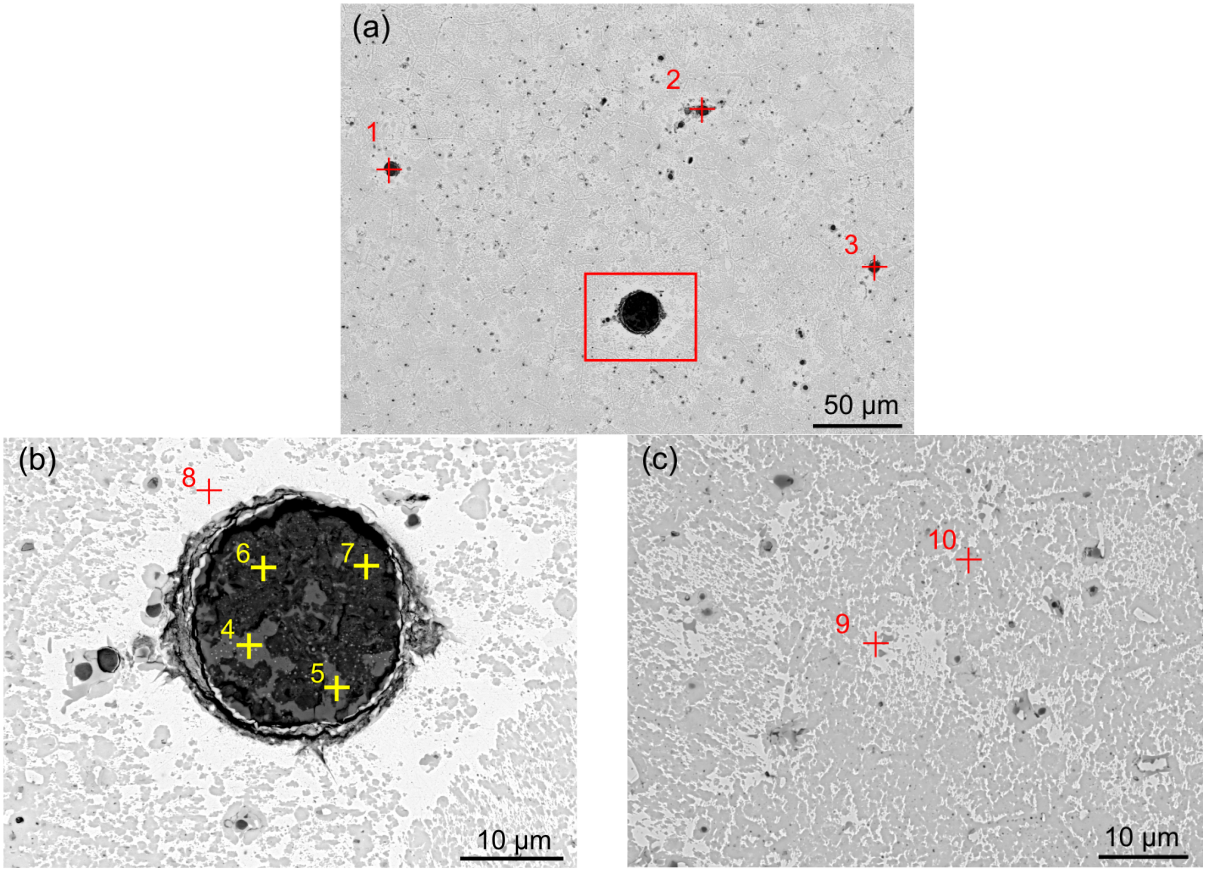

Figure 5. SEM BSE images of annealed UPdLn. The red rectangle in Figure 5a indicates the location of the magnified image shown in Figure 5b. The magnified image for fuel matrix is shown in Figure 5c. EDS data are listed in Table 5.

Table 5. EDS data for the points shown in Figure 5. Values in at. %.

	U	Pd	Nd	Ce	Pr	La	Phase[a]
1	6	56	17	14	6	1	Pd_3Ln_2/Pd_4Ln_3
2	7	57	13	18	5	1	Pd_3Ln_2/Pd_4Ln_3
3	7	57	14	16	5	1	Pd_3Ln_2/Pd_4Ln_3
4	6	57	14	17	5	1	Pd_3Ln_2/Pd_4Ln_3

5	6	58	14	16	5	1	Pd_3Ln_2/Pd_4Ln_3
6	8	79	5	6	2	1	
7	8	82	4	4	1	0	
8	99	1	0	0	0	0	α-U
9	99	1	0	0	0	0	α-U
10	99	1	0	0	0	0	α-U

[a] Suggested phase based on the SEM EDS analysis.

3.2.2. Diffusion between UPdLn and Fe

The diffusion interface between the UPdLn alloy and Fe is shown in Figure 6, with EDS data listed in *Table 6*. The interface with the alloy matrix and Pd-Ln precipitates are shown in Figure 6b and Figure 6c, respectively.

The EDS line spectrum, indicated by the arrow in Figure 6b and shown in Figure 6d, indicates the Fe diffusion roughly 20 μm into the UPdLn alloy matrix, forming two diffusion regions and decreasing with diffusion depth. The first diffusion region is dark grey, at a distance of 10-20 μm. The Fe content decreases from 14 at. % to 5 at. % with the diffusion depth, shown in the EDS line spectrum in Figure 6d. The Pd in this region is only 1-2 at. % (points 1-4 in Figure 6b and *Table 6*). Nanostructures/precipitates, as in the UPd diffusion region shown in Figure 3, are also present in this region. There appears to be a thin layer (points 3-4) above the bottom layer (points 1-2) in the region. The compositions between the two layers do not exhibit any differences, based on the EDS analysis.

The second diffusion region is at the distance of 20-30 μm with less Fe, while the composition of U and Pd (points 5-6 in Figure 6b and *Table 6*) is almost the same as the matrix. The diffusion region has fewer grey phases than the alloy matrix, which are indicated by red arrows in Figure 6b.

Between the two diffusion regions are black precipitates, comprised of ~ 48U-48Pd-4Fe at. %, based on the EDS analysis (points 5-6 in Figure 6b and *Table 6*). The composition is likely to be UPd. However, UPd is a high temperature compound and forms above 1242 K [16], so it should not be present in this diffusion couple run at 873 K. Note that the black precipitates are extremely small (roughly 1 μm), U from the surrounding matrix could contribute to the X-ray counts, artificially raising the measured content of U. Therefore, the precipitates are more likely to be UPd_3.

The diffusion of UPdLn into the Fe was not observed. The interface between UPdLn and Fe, as shown in Figure 6b, is flat and straight, which indicates the original contact surface. On the Fe side, there is no U, Pd, or Ln observed, and thus UPdLn did not diffuse into Fe.

A Pd-Ln precipitate is shown at the interface in Figure 6c. There is no indicator of any Pd or Ln diffusion into Fe. The precipitate is comprised of ~ 17Pd-70Ln-8U-5Fe at. %, based on the EDS analysis (point 1 in Figure 6c and *Table 6*). There is slightly less Fe in the precipitate than was found in the diffusion region shown in Figure 6b, which has 7-8 at. % Fe (points 1-4 in Figure 6b). The other Pd-Ln precipitates that are 10-20 μm away from the interface contain much less Fe, only 1-2 at. % (points 2-4 in Figure 6c and *Table 6*). Diffusion of Fe appears to be slightly more favorable towards the alloy matrix as opposed to diffusion into the precipitates.

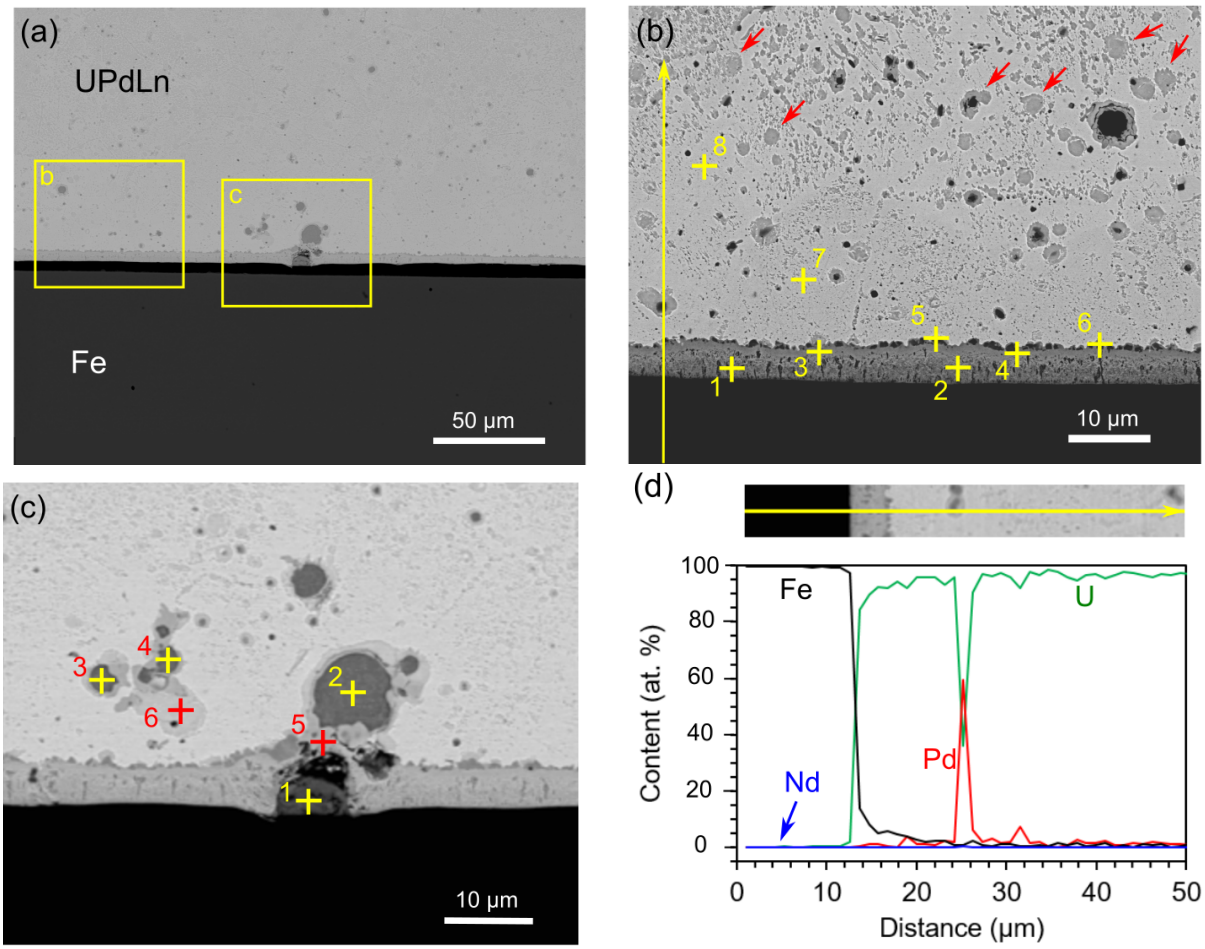

Figure 6. (a) SEM image of the UPdLn/Fe interface. The yellow rectangle b indicates the magnification present in Figure 6b, and the yellow rectangle c indicates the magnification present in Figure 6c. The yellow arrow in Figure 6b indicates the EDS line spectrum in *Figure 6*d. The EDS point data are listed in *Table 6*.

Table 6. SEM EDS data for the points shown in Figure 6. Values in at. %.

	U	Pd	Nd	Ce	Pr	La	Fe	Phase[a]
			Figure 6b					
1	87	1	0	3	1	2	7	
2	92	1	0	0	0	0	8	
3	92	1	0	1	1	0	5	
4	92	2	1	0	0	0	5	
5	48	48	0	0	0	0	4	
6	52	42	1	1	1	1	3	
7	91	3	0	1	2	0	4	
8	96	2	0	0	1	0	0	
			Figure 6c					
1	8	17	26	32	11	2	5	
2	6	59	13	16	5	0	1	Pd_3Ln_2/Pd_4Ln_3
3	6	54	16	14	8	1	2	Pd_3Ln_2/Pd_4Ln_3

4	8	56	15	13	5	2	1	Pd_3Ln_2/Pd_4Ln_3
5	85	4	2	3	2	0	3	
6	94	0	0	1	1	0	3	

[a] Suggested phase based on the SEM EDS analysis.

3.3. USn

3.3.1. Alloy microstructure

The microstructures of as-cast and annealed USn are shown in Figure 7 and Figure 8, respectively. The alloy matrix is U, and almost free of Sn. The 2-3 at. % Sn in the matrix, as indicated by the EDS data points 5-7 for Figure 7 and points 1-2 for Figure 8, is possibly due to the EDS quantification uncertainty. A representative EDS energy spectrum of the alloy is shown in Figure 8c. Note that the X-ray emission peaks of U and Sn are 3.356 and 3.443 keV, respectively. These energy peak shoulders are overlapped, thus resulting in the uncertainty of EDS quantification. In addition, the uncertainty of the Sn-containing alloy is greater than the Pd-containing alloy because the main X-ray emission peak of Pd is 2.838 keV, which is well separated from U.

Precipitates are randomly dispersed in the alloy matrix, and the microstructure is not changed after annealing. The precipitate distribution is not perfectly uniform over the sample, as shown in Figure 8a, due to element distribution and solidification after casting. Although the button was re-melted three times to enhance element homogeneity, it cannot be ensured. The density of the phases formed, the miscibility of the phases with U, and the cooling rate of the alloy after casting the pin all contribute to the homogeneity of the final alloy. The heterogeneity present is not significant and does not affect the microstructure analysis, though. EDS data for both the as-cast and annealed structures are listed in Table 7. The precipitate composition in as-cast USn alloy is 67U-33Sn at. %, and does not change after annealing. The composition indicates the ratio of U-to-Sn is 2, which is not a ratio of any known compound based on the phase diagram between U and Sn [18]. Although the U from the surrounding matrix may raise the X-ray counts of U, it is not the case for U-Sn precipitates due to the relatively large size (above 5 μm). The consistent EDS data for the precipitates indicate an unknown intermetallic compound of U_2Sn. Although as mentioned the energy peak shoulders of U and Sn are overlapped, the effect on the precipitates is less significant than the fuel matrix owing to the fact that larger amounts of Sn are in the precipitates.

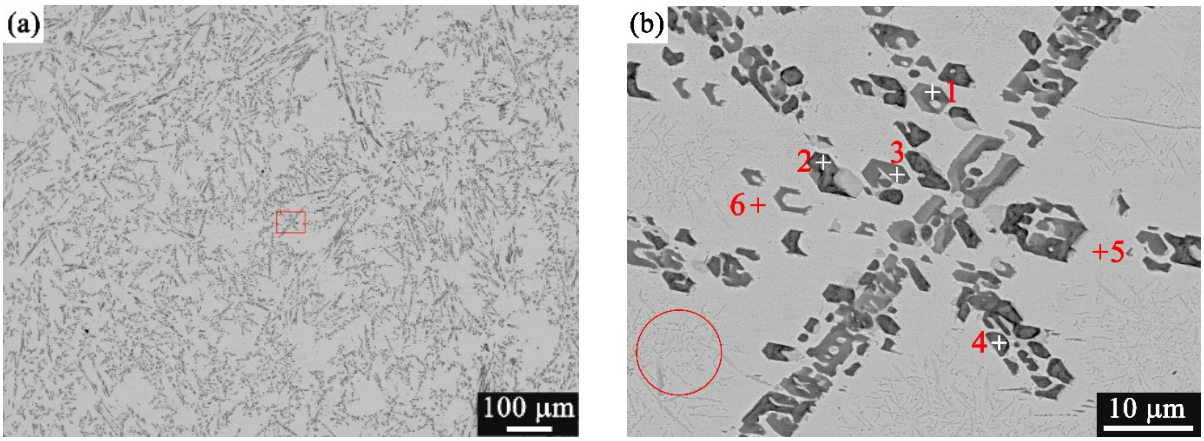

Figure 7. SEM BSE images of as-cast USn. The red rectangle in Figure 7a indicates the location of the magnified image shown in Figure 7b. The red circle in Figure 7b highlights the fine structure present in the microstructure. EDS data are listed in Table 7.

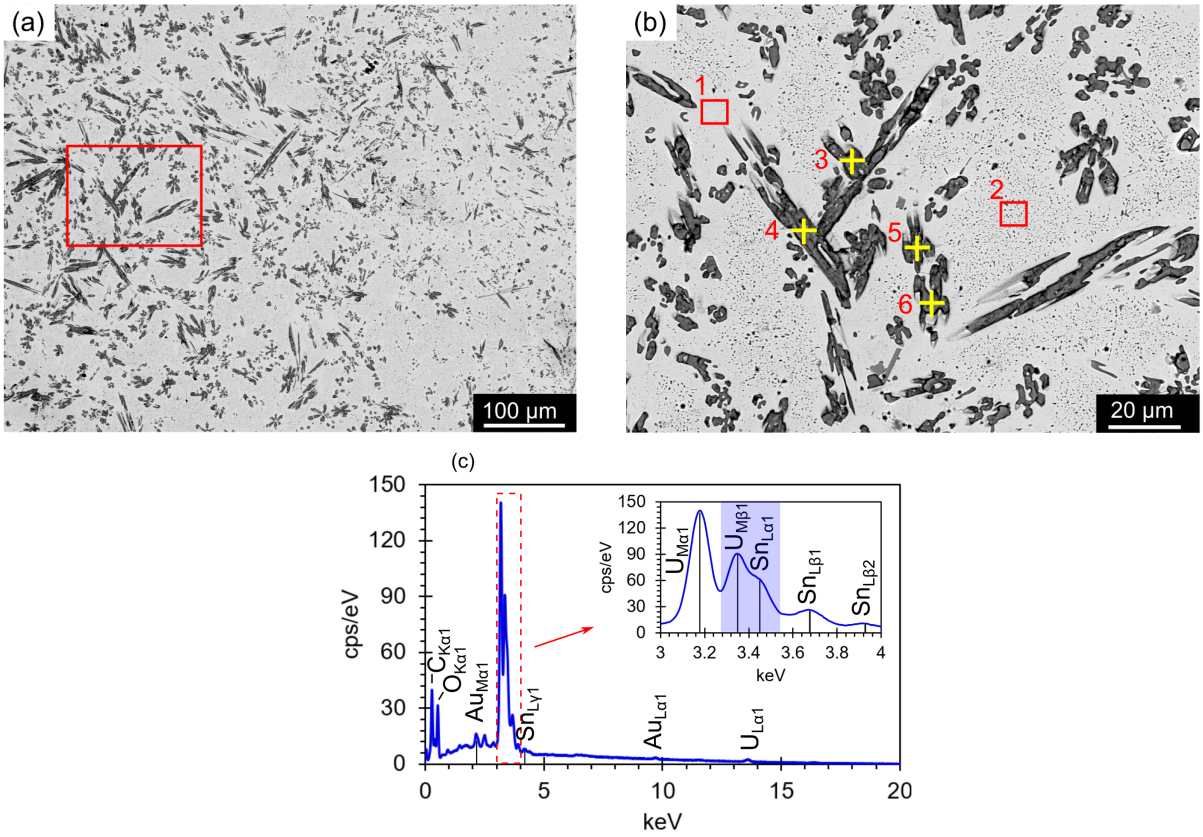

Figure 8. SEM BSE images of annealed USn. The red rectangle in Figure 8a indicates the location of the magnified image shown in Figure 8b. EDS data are listed in Table 7. Figure 8c shows the overlap in the U and Sn energy peaks.

Table 7. EDS data for the points and boxes shown in Figure 7b and Figure 8b. Values in at. %.

	Figure 7b				Figure 8b		
	U	Sn	Phase[a]		U	Sn	Phase[a]
1	68	32	U_2Sn	1	98	2	
2	67	33	U_2Sn	2	97	3	
3	67	33	U_2Sn	3	66	34	U_2Sn
4	62	38	U_2Sn	4	69	31	U_2Sn
5	98	2	α-U	5	67	34	U_2Sn
6	98	3	α-U	6	66	34	U_2Sn

[a] Suggested phase based on the SEM EDS analysis.

3.3.2. Diffusion between USn and Fe

The diffusion interface between USn and Fe is shown in Figure 9, with EDS data listed in Table 8. The EDS line spectrum, shown in Figure 9c, indicates the Fe diffusion roughly 60 μm into the USn matrix, forming a dark grey layer (at the distance 30-90 μm). The Fe content in the diffusion layer decreases with the diffusion depth. Conversely, the diffusion of USn into the Fe was not observed. As shown in Figure 9a and b, the interface between USn and Fe is straight which indicates the original contact surface. On the Fe side, there is no U or Sn observed, so diffusion is only from Fe into the USn alloy.

The EDS line spectrum, at the distance 80-90 μm, together with the EDS map of Sn (inset of Figure 9b), indicate Sn is enriched at the interface between the diffusion region and USn matrix, while the bulk of the diffusion region contains only trace amounts of Sn. Although the U-Sn precipitates are evenly distributed throughout the matrix, none are observed in the diffusion region. This indicates that the interaction between U and Fe is more favorable than that between U and Sn, so the U-Sn precipitates are decomposing, with Sn being pushed along the diffusion front.

Based on the EDS data listed in Table 8, the diffusion zone contains about 93 at. % U and 5 at. % Fe. Such a composition does not match any known intermetallic compound in the U-Fe binary system [19]. The previous study has revealed the U-rich compound, U_6Fe, could form on the fuel side [9], however it was not observed in the diffusion zone of the present result. It indicates, the reaction condition, i.e., the time and temperature, is insufficient for the formation of U-Fe phases. The reaction between U and Fe forming U-Fe phases has not yet occurred.

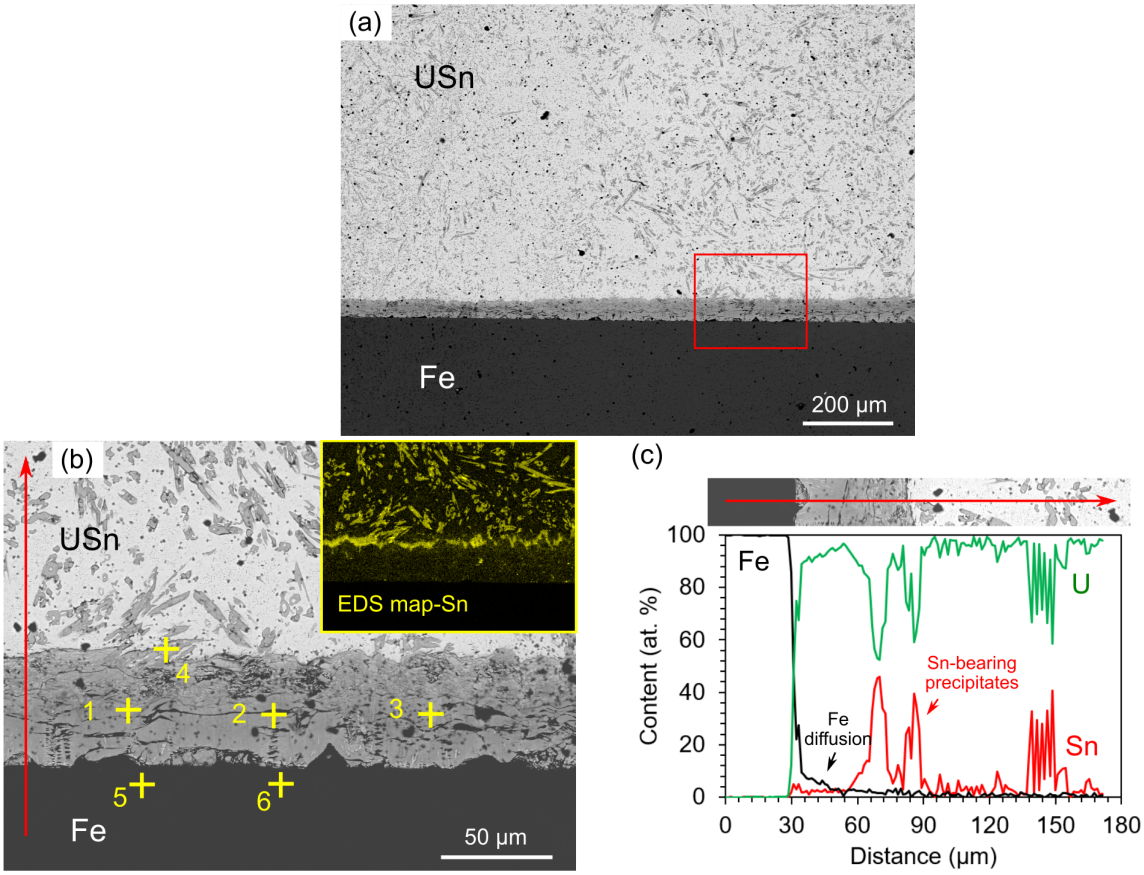

Figure 9. SEM BSE images of USn/Fe interface. The red rectangle in Figure 9a indicates the location of magnified image shown in Figure 9b. The EDS map of Sn is present, in Figure 9b, to show the distribution of Sn. The red arrow in Figure 9b indicates the EDS line spectrum in Figure 9c. The EDS data are listed in Table 8.

Table 8. EDS data for the points in Figure 9b. Values in at. %.

	U	Sn	Fe
1	93	2	5
2	93	3	4
3	92	2	5
4	61	37	2
5	0	0	100
6	0	0	100

3.4. USnLn

3.4.1. Alloy microstructure

The microstructures of as-cast and annealed USnLn alloy are shown in Figure 10 and Figure 11, with EDS data provided in Table 9, respectively. Precipitates are randomly dispersed in the alloy matrix, and their microstructure and composition did not change after annealing. The fuel matrix, points 9-10 in Figure 10 and points 5-6 in Figure 11, contains ~98 at. % U and 2 at. % Sn, which is the same as the USn alloy matrix. The dark grey phase/precipitates, points 1-2 and 4 in Figure 10 and points 1-4 in Figure 11, contain ~ 45 Sn, 45 Ln and 10 U in at. %. Such a composition indicates the SnLn phase, which is a known binary phase in the Sn-Nd/Ce/Pr/La systems. The measured U content, 10 at. % U, may be dissolved U in the phase or U from the surrounding matrix contributed to the X-ray counts. In the SnLn phase, the lanthanide composition, roughly 24Nd-11Ce-7Pr-3La at. % based on the EDS analysis, is consistent with the Ln composition cast into the alloy, i.e., 52.3Nd-25.4Ce-16.2Pr-6.1La at. %. This result indicates Sn has the same preference binding each lanthanide in the ratio of 1:1.

The smaller precipitates in grey, points 5-8 in Figure 10 and arrows 7-8 in Figure 11, roughly contain 80 U and 20 Sn in at. %. Analyzed by EDS, the compositions of these precipitates are consistent, so they are likely to be a U-Sn binary phase. However, this composition is not one of the known phases in the U-Sn system, so it could be an unknown U-rich U-Sn phase. In addition, this composition might be affected by the SEM-EDS limitation as the grey precipitates are smaller than the interaction volume from the beam. The U from the surrounding matrix contributes to the X-ray counts and artificially raises the U content. It's possible the precipitates are in the composition of U_2Sn as observed in the USn alloy. As mentioned in Section 2, the alloy composition is 86.3U-7.5Sn-6.2Ln at. %. The EDS results indicates the Sn and Ln combine and form the 1:1 phase and the extra Sn remains in the fuel matrix, forming a U-Sn phase.

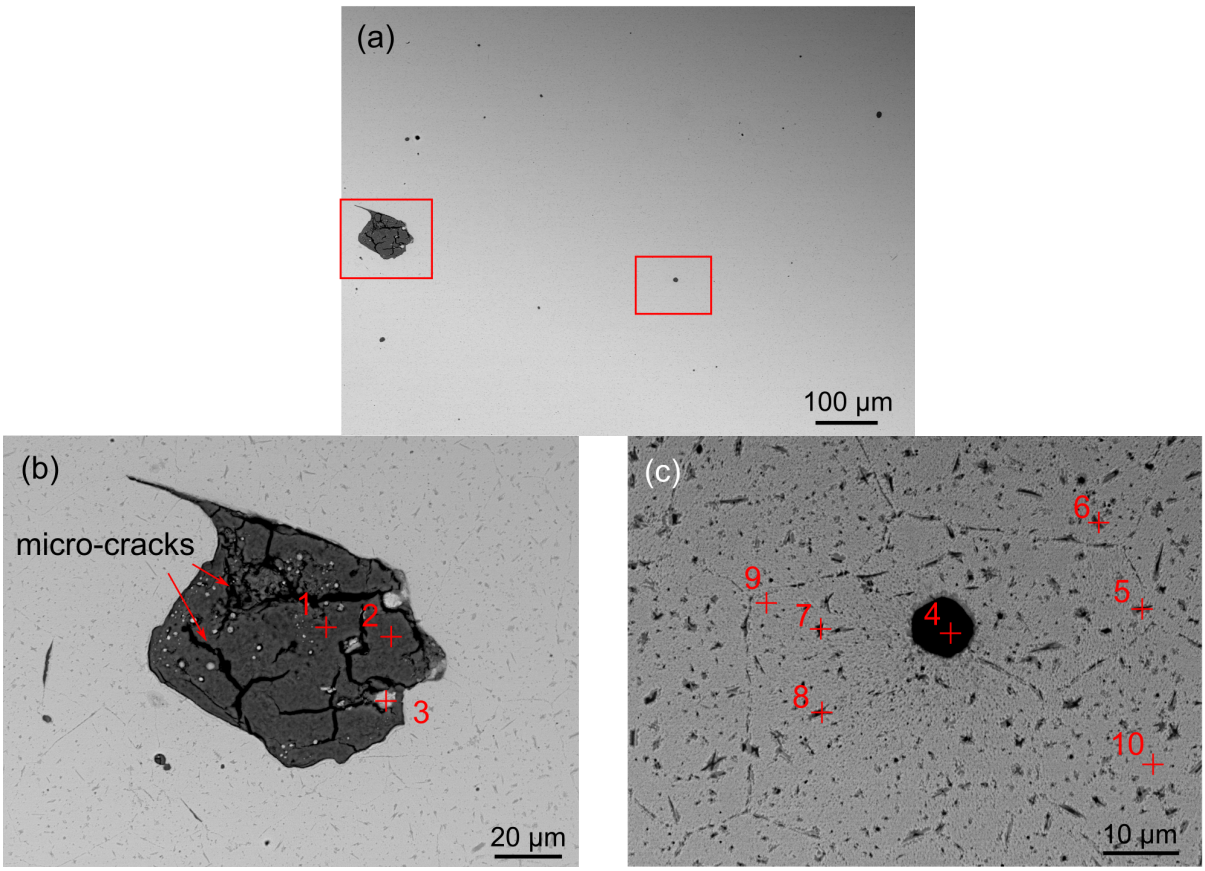

Figure 10. SEM BSE images of as-cast USnLn. The red rectangles in Figure 10a indicate the location of the magnified image shown in Figure 10b and c. EDS data are listed in Table 9. The image contrast and brightness in Figure 10c are set differently than others to discern the small randomly dispersed precipitates in the fuel matrix (points 5-8).

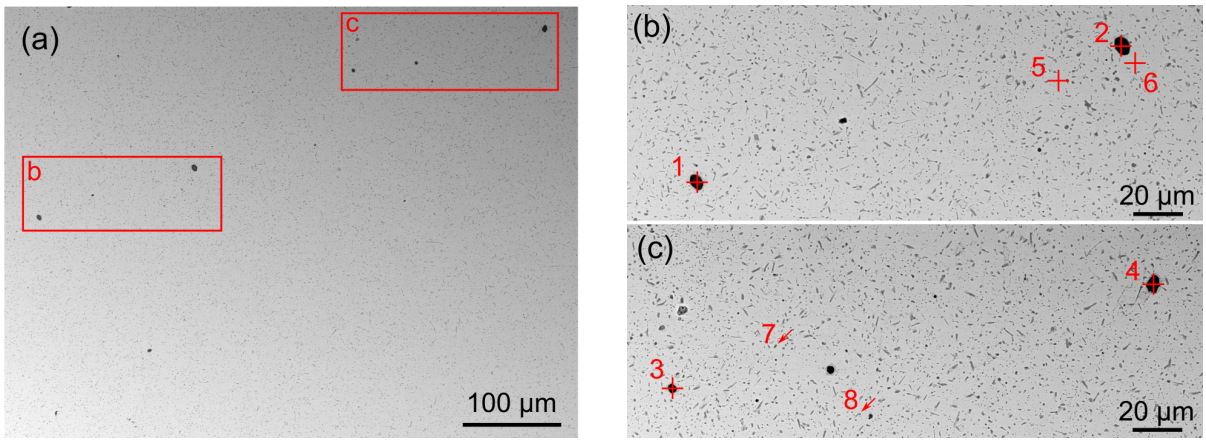

Figure 11. SEM BSE images of annealed USnLn. The red rectangles in Figure 11a indicate the location of the magnified images shown in Figure 11b and c. EDS data are listed in Table 9. The arrows 7-8 point at the small precipitates in the fuel matrix.

Table 9. EDS data for the points and arrows shown in Figure 10 and Figure 11. Values in at. %

	U	Sn	Nd	Ce	Pr	La	Phase[a]

			Figure 10				
1	7	48	24	11	7	3	SnLn
2	8	47	24	11	7	3	SnLn
3	96	2	1	0	1	0	
4	9	49	22	11	7	2	SnLn
5	79	21	0	0	0	0	
6	85	15	0	0	0	0	
7	79	21	0	0	0	0	
8	75	25	0	0	0	0	
9	98	2	0	0	0	0	
10	98	2	0	0	0	0	
			Figure 11				
1	9	46	24	11	7	3	SnLn
2	9	45	24	12	8	2	SnLn
3	10	45	23	11	7	4	SnLn
4	11	44	24	11	8	2	SnLn
5	96	1	0	1	1	1	
6	98	1	0	1	0	0	
7	83	16	0	1	0	0	
8	81	18	0	0	1	0	

[a] Suggested phase based on the SEM EDS analysis.

3.4.2. Diffusion between USnLn and Fe

The diffusion interface between USnLn and Fe is shown in Figure 12, with line scan locations indicated by the red arrows. The EDS line spectrum across the USnLn matrix, indicated by the red arrow b in Figure 12a and shown in Figure 12b, illustrates the Fe diffusion more than 30 μm into the matrix (at the distance 10-40 μm), with the Fe content in the diffusion zone decreasing with the diffusion depth. At the distance 11-12 μm in Figure 12b, the Fe content slightly increases due to the formation of the grey layer at interface. On the other hand, the diffusion of USnLn into Fe was not observed. The interface between USnLn and Fe is flat and straight, which indicates the original contact surface. Since there is no U, Sn, or Ln observed on the Fe side, USnLn did not diffuse into the Fe. The other EDS line spectrum, across the Sn-Ln precipitates, indicated by the red arrow c in Figure 12a and shown in Figure 12c, shows Fe slightly decreases at the Sn-Ln precipitate (at the distance 14 μm). It is not zero as the surrounding Fe contributed to the X-ray counts. The Sn-Ln precipitates did not diffuse toward Fe as Sn and Ln were not observed on the Fe side.

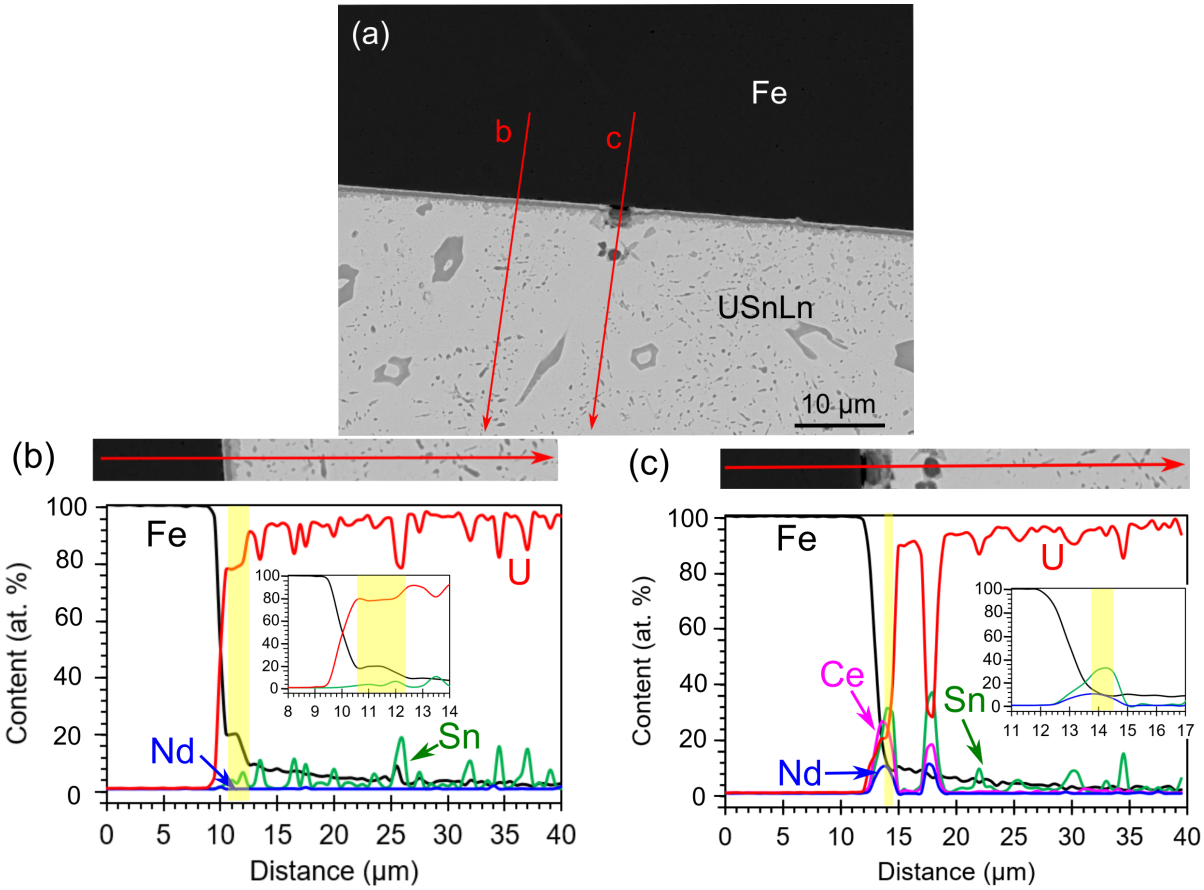

Figure 12. SEM BSE image with EDS line spectra showing the diffusion interface between USnLn and Fe. Figure 12b is the EDS line spectrum of matrix-Fe diffusion showing the distribution of Fe, U, Sn, and Nd. The magnified spectrum showing the distribution of Fe, U, and Sn within the distance 8-14 μm is embedded. Figure12c is the EDS line spectrum of precipitate-Fe diffusion showing the distribution of Fe, U, Sn, Nd, and Ce. The magnified spectrum showing the distribution of Fe, Sn, and Nd within the distance 11-17 μm is embedded. The contents of Pr and La in the precipitate are not zero, but too small to display in the spectrum.

4. Discussion

4.1 Phases in UPd and USn alloys

Based on EDS analysis, UPd_3 is the binary phase in the UPd alloy. The result is consistent with the U-Pd binary phase diagram [16], where the alloy composition falls between UPd_3 and U phases at the investigated temperature. U_2Sn is the suspected binary phase in the USn alloy. U_2Sn has not been reported in the literature, and the crystal structure and thermodynamic properties are unknown. Further investigation of this possible phase is in progress.

Nanometer-sized Pd-precipitates are present in the UPd and UPdLn alloy matrixes. They are transformed from the solid solute Pd in U when the alloy is cooled from the elevated temperature after melting. The solid solubility of Pd in U is up to 5 at. % at elevated temperature, and almost 0 at. % at room temperature, based on the U-Pd binary phase diagram [16]. When the alloy is cooled the solid solution is not able to hold all the Pd atoms that are dissolved in U, so the Pd atoms precipitate. The EDS date, listed in Table 2 and Table 4, support that the alloy matrix

contains roughly 2-5 at. % Pd. However, the USn and USnLn alloys exhibit trace amounts of Sn-precipitates in the matrix. The solid solubility of Sn in U is negligible at all temperatures, based on the U-Sn binary phase diagram [18]. The EDS data, provided in Table 7, indicate 2-3 at. % Sn in the alloy matrix; although the Sn energy peak overlaps with the U peak, so the Sn content is artificially raised. The actual Sn content in the matrixes for USn and USnLn alloys is much less than that of Pd for UPd and UPdLn alloys.

4.2. Phases in UPdLn and USnLn alloys

The UPdLn alloy (85.5U-8.3Pd-6.2Ln at. %) contains more Pd than Ln. The observed binary phases are LnPd and Pd-rich phases Pd_4Ln_3 or Pd_3Ln_2 based on the EDS composition. The formation of the Pd-rich phases is due to the excess of Pd over Ln. The result is consist with the previous study [13] on the 61.9U-24.5Zr-7.0Pd-6.6Ln at. % alloy, in which the main Pd-Ln phase is LnPd. Note that Pd_4Ln_3 is a known phase in the phase diagrams [20][21][22], however the Pd_3Ln_2 type phase is not known. Nevertheless, a previous TEM study has observed the composition for Pd_3Ln_2 with a diffraction pattern that could not be indexed [13]. That result indicates the existence of a Pd-rich Pd-Ln phase that has not been characterized and is not included in the current phase diagram. Fully characterizing this phase is outside the present scope.

The USnLn alloy (86.3U-7.5Sn-6.2Ln at. %) contains 1:1 SnLn phase. As with the UPdLn alloy, the additive, in this case Sn, is in excess of lanthanides. However, the extra Sn does not form Sn-rich Sn-Ln phases, but instead binds with U forming the suspected U-rich U-Sn phase. The previous study [8] on the 65.4U-21.1Zr-7.0Sn-6.5Ln at. % alloy also reveals that the resulting phases are Ln-rich Ln-Sn and Zr-rich Zr-Sn. On the Sn-Nd/Ce/Pr/La phase diagrams [23][24][25][26], the maximum melting temperature phases are on the lanthanide-rich side. Therefore, only the higher melting, so presumably more stable, Sn-Ln compounds are forming. This qualitatively indicates that the U-Sn phase has a stability between the Sn-rich Sn-Ln phases and the observed phase (SnLn). This is advantageous, since the excess Sn still bound to U is available for further Ln loading. This raises the question in UPdLn alloy, will the Pd-rich Pd-Ln phases decompose to accommodate more Ln loading, or has the capacity of the additive been reached? This would imply that anytime there is an excess of Pd present, i.e. as lanthanides are produced during irradiation, Pd-rich compounds will form, decreasing the loading capacity of the additive.

4.3. Diffusion behavior

The diffusion regions observed in these diffusion couple samples are mainly formed by the diffusion between U and Fe. The result is in accordance with previous isothermal diffusion couple tests of the fuel-cladding system which are dominated by U-Fe diffusion [9][27]. Generally, such a diffusion would form FeU_6 and Fe_2U on the fuel and cladding sides, separately. The enthalpies of formation of FeU_6 and Fe_2U are negative, and Gibbs free energies of formation are more negative, as listed in Table 10. Despite the strong driving force for formation, FeU_6 and Fe_2U were rarely observed in the current work. However, previous studies [27][28] have observed FeU_6 and Fe_2U forming under similar condition as the present work, indicating that Fe diffusion into U was hindered by the Pd- or Sn-bearing precipitates dispersed in the U-Pd and U-Sn alloys.

The nanometer-sized Pd-precipitates present in the UPd and UPdLn alloys matrix slowed down Fe diffusion. The Pd-precipitates might diffuse and react with the Fe, due to the negative Gibbs free energy of formation of Fe-Pd compounds at 873 K [17], as listed in Table 10.

However, the free energy is greater than Fe-U compounds' free energy at the same temperature. In other words, the Fe-U compounds are more thermodynamically stable than Fe-Pd compounds, so Fe prefers to combine with U over Pd. The Pd-precipitates therefore offer some resistance to Fe diffusion into the alloy matrix.

The UPd_3 and U-Sn compounds in the UPd and USn alloys also preclude Fe diffusion. The SEM images and EDS line spectra, shown in Figure 3 and *Figure 9*, indicate the compounds are stable toward Fe. The UPd_3 and U-Sn compounds are more thermodynamically stable than Fe-U compounds. Despite of the fact that thermodynamic data of U-Pd and U-Sn compounds are lacking, indications are available based on the limited thermodynamic data in the literature. The suspected U_2Sn compound, instead of USn_3, was observed in the USn alloy, which indicates U_2Sn is more stable than USn_3. The enthalpy of formation for USn_3 is equal to that of Fe_2U and more negative than FeU_6 as listed in Table 10. These two factors justify the suspected U_2Sn is even more stable than Fe_2U and FeU_6. In addition, the enthalpy of formation for UPd_3 is more negative than Fe_2U and FeU_6, indicating a higher thermodynamic stability. Such stable phases are not likely to diffuse or react with Fe. Therefore, they offer a barrier, though discontinuous, to Fe diffusion.

Fe diffusion into the UPd and UPdLn matrixes are both roughly 20 μm in depth shown in Figure 3 and Figure 6, respectively; however, the microstructures of the diffusion regions appear different. The dark UPd_3 intergranular precipitates in UPd alloy mitigated Fe diffusion. The intergranular structure is an interface between diffusion and non-diffusion regions as shown in Figure 3; in other words, the UPd_3 intergranular precipitates hinder Fe diffusion. This phenomenon was not observed in the UPdLn diffusion couple owing to the fact that UPd_3 compounds are not present in the alloy.

Dark nanostructures/precipitates are in the diffusion regions for both UPd and UPdLn alloys. These nanostructures may be Pd-Fe compound; however, they cannot be identified by EDS with SEM due to their small size. The concentration of the dark nanostructures is higher closer to the interface and decreases the further away from the interface due to a decreasing Fe content along the diffusion path. In the UPdLn diffusion couple, the dark precipitates (points 5-6 in Figure 6b), suspect to be UPd_3, were the Pd-precipitates pushed away from the interface due to the diffusion of Fe and combined with U, forming the suspected UPd_3 phase. Similar phenomenon has been observed in the USn alloy (see Figure 9b) where U-Sn precipitates decomposed due to the diffusion of Fe, with Sn pushed along the diffusion front. In both cases, the additive element, Sn or Pd, is pushed against their concentration gradient, away from the interface. The formation of thermodynamically stable U-Fe intermetallics is likely the driving force. The need to push these elements away from the diffusion zone maybe hindering Fe diffusion into the fuel.

Regarding the USnLn and UPdLn alloys, Fe diffusion with the Sn-Ln and Pd-Ln phases is minor, in comparison with the diffusion of alloy matrix, U. It is well known Fe diffusion with Ln is significant, which is of importance to the adverse lanthanide-induced FCCI. However, in this work, the diffusion is negligible owing to the dopants, Sn and Pd, added into the fuel alloys.

Table 10. Summary of the thermodynamic data available in the literature (unit: kJ/g-atom).

Phase	UPd_3	USn_3	Fe_2U	FeU_6	FePd	$FePd_3$	FeSn	$FeSn_2$	NdPd	Nd_5Sn_3
Enthalpy of formation at 298 K	-61 [29]	-23 [30]	-23 [31]	-13 [31]	-13.7 [17]	-22 [17]	-28 [32]	-23 [32]	-67[b] [33]	-74 [34]

Gibbs free energy of formation at 873 K[a]	N/A	N/A	-59 [31]	-59 [31]	-13 [17]	-19 [17]	-9 [32]	-7 [32]	N/A	N/A

a. Standard reference state for each pure element of the phase.
b. 640 K.

5. Conclusion

The microstructure and diffusion behavior of UPd, UPdLn, USn, and USnLn were analyzed with SEM and EDS analysis. The following conclusions can be drawn from this work:

- UPd_3 compound forms in the UPd alloy. The UPd_3 intergranular precipitates were observed to hinder Fe diffusion. The U-Sn compound is suspected to be U_2Sn, but this phase is unknown in the literature. Study of this phase is in progress.
- In the UPdLn and USnLn alloys, additives Pd and Sn are in excess of Ln. PdLn compound and Pd-rich compounds (Pd_4Ln_3 and Pd_3Ln_2) are present in the UPdLn alloy. SnLn and suspected U_2Sn are present in the USnLn alloy. The excess Sn still bound to U allows further Ln loading, while Pd-rich compounds may decrease the loading capacity of Pd. Therefore, Sn is a more promising additive.
- The diffusion of Fe could push the nanometer-sized Pd-precipitates and the Sn that is decomposed from the U-Sn precipitates away from the interface, forming suspected UPd_3 and U_2Sn at the diffusion front of Fe.
- The diffusion regions are primarily formed by the diffusion between U and Fe. The compounds diffusion is insignificant. Therefore, it's deduced the lanthanide-induced FCCI would be mitigated as Pd and Sn could stabilize the lanthanides produced for burnup.

Acknowledgement

This work was supported by the U.S. Department of Energy, Office of Nuclear Energy under DOE Idaho Operations Office Contract DE-AC07-05ID14517. Accordingly, the U.S. Government retains and the publisher, by accepting the article for publication, acknowledges that the U.S. Government retains a nonexclusive, paid-up, irrevocable, worldwide license to publish or reproduce the published form of this manuscript or allow others to do so, for U.S. Government purposes.

References

[1] R.D. Mariani, D.L. Porter, S.L. Hayes, J.R. Kennedy, Metallic Fuels: The EBR-II Legacy and Recent Advances, Procedia Chem. 7 (2012) 513–520.

https://doi.org/10.1016/J.PROCHE.2012.10.078.
[2] W.J. Carmack, H.M. Chichester, D.L. Porter, D.W. Wootan, Metallography and fuel cladding chemical interaction in fast flux test facility irradiated metallic U-10Zr MFF-3 and MFF-5 fuel pins, J. Nucl. Mater. 473 (2016) 167–177. https://doi.org/10.1016/J.JNUCMAT.2016.02.019.
[3] L.C. Walters, Thirty years of fuels and materials information from EBR-II, J. Nucl. Mater. 270 (1999) 39–48. https://doi.org/10.1016/S0022-3115(98)00760-0.
[4] D.C. Crawford, D.L. Porter, S.L. Hayes, Fuels for sodium-cooled fast reactors: US perspective, J. Nucl. Mater. 371 (2007) 202–231. https://doi.org/10.1016/J.JNUCMAT.2007.05.010.
[5] Y. Xie, J. Zhang, X. Li, J.P. Isler, M.T. Benson, R.D. Mariani, C. Unal, Lanthanide migration and immobilization in metallic fuels, Prog. Nucl. Energy. 109 (2018) 233–238. https://doi.org/10.1016/J.PNUCENE.2018.08.019.
[6] M.T. Benson, Y. Xie, J.A. King, K.R. Tolman, R.D. Mariani, I. Charit, J. Zhang, M.P. Short, S. Choudhury, R. Khanal, N. Jerred, Characterization of U-10Zr-2Sn-2Sb and U-10Zr-2Sn-2Sb-4Ln to assess Sn+Sb as a mixed additive system to bind lanthanides, J. Nucl. Mater. 510 (2018) 210–218. https://doi.org/10.1016/J.JNUCMAT.2018.08.017.
[7] M.T. Benson, J.A. King, R.D. Mariani, Investigation of Tin as a Fuel Additive to Control FCCI, in: TMS 2018 147th Annu. Meet. Exhib. Suppl. Proc., 2018: pp. 695–702.
[8] M.T. Benson, J.A. King, R.D. Mariani, M.C. Marshall, SEM characterization of two advanced fuel alloys: U-10Zr-4.3Sn and U-10Zr-4.3Sn-4.7Ln, J. Nucl. Mater. 494 (2017) 334–341. https://doi.org/10.1016/J.JNUCMAT.2017.07.057.
[9] Y. Xie, M.T. Benson, L. He, J.A. King, R.D. Mariani, D.J. Murray, Diffusion behaviors between metallic fuel alloys with Pd addition and Fe, J. Nucl. Mater. 525 (2019) 111–124. https://doi.org/10.1016/j.jnucmat.2019.07.028.
[10] Y. Xie, M.T. Benson, L. He, J.A. King, Diffusion behaviors between Fe and Pd-containing metallic fuel, Trans. Am. Nucl. Soc. 120 (2019) 412–413.
[11] M.T. Benson, Y. Xie, L. He, K.R. Tolman, J.A. King, J.M. Harp, R.D. Mariani, B.J. Hernandez, D.J. Murray, B.D. Miller, Microstructural characterization of annealed U-20Pu-10Zr-3.86Pd and U-20Pu-10Zr-3.86Pd-4.3Ln, J. Nucl. Mater. 518 (2019) 287–297. https://doi.org/10.1016/j.jnucmat.2019.03.014.
[12] M.T. Benson, L. He, J.A. King, R.D. Mariani, A.J. Winston, J.W. Madden, Microstructural characterization of as-cast U-20Pu-10Zr-3.86Pd and U-20Pu-10Zr-3.86Pd-4.3Ln, J. Nucl. Mater. 508 (2018) 310–318. https://doi.org/10.1016/J.JNUCMAT.2018.05.062.
[13] M.T. Benson, L. He, J.A. King, R.D. Mariani, Microstructural characterization of annealed U-12Zr-4Pd and U-12Zr-4Pd-5Ln: Investigating Pd as a metallic fuel additive, J. Nucl. Mater. 502 (2018) 106–112. https://doi.org/10.1016/J.JNUCMAT.2018.02.012.
[14] R.D. Mariani, D.L. Porter, T.P. O'Holleran, S.L. Hayes, J.R. Kennedy, Lanthanides in metallic nuclear fuels: Their behavior and methods for their control, J. Nucl. Mater. 419 (2011) 263–271. https://doi.org/10.1016/J.JNUCMAT.2011.08.036.
[15] J.M. Harp, D.L. Porter, B.D. Miller, T.L. Trowbridge, W.J. Carmack, Scanning electron microscopy examination of a Fast Flux Test Facility irradiated U-10Zr fuel cross section clad with HT-9, J. Nucl. Mater. 494 (2017) 227–239. https://doi.org/10.1016/J.JNUCMAT.2017.07.040.
[16] H. Kleykamp, S.G. Kang, The constitution of the uranium-tin-palladium system, J. Nucl. Mater. 230 (1996) 280–286. https://doi.org/10.1016/0022-3115(96)00161-4.
[17] G. Ghosh, C. Kantner, G.B. Olson, Thermodynamic modeling of the Pd-X

(X=Ag, Co, Fe, Ni) systems, J. Phase Equilibria. 20 (1999) 295–308. https://doi.org/10.1361/105497199770335811.
[18] A. Palenzona, P. Manfrinetti, The phase diagram of the U-Sn system, J. Alloys Compd. 221 (1995) 157–160. https://doi.org/10.1016/0925-8388(94)01463-9.
[19] M. Kurata, T. Ogata, K. Nakamura, T. Ogawa, Thermodynamic assessment of the Fe–U, U–Zr and Fe–U–Zr systems, J. Alloys Compd. 271–273 (1998) 636–640. https://doi.org/10.1016/S0925-8388(98)00176-5.
[20] H. Okamoto, Nd-Pd (neodymium-palladium), J. Phase Equilibria. 13 (1992) 220–222. https://doi.org/10.1007/BF02667499.
[21] H. Okamoto, Ce-Pd (cerium-palladium), J. Phase Equilibria. 12 (1991) 700–701. https://doi.org/10.1007/BF02645180.
[22] H. Okamoto, Pd-Pr (Palladium-Praseodymium), J. Phase Equilibria. 14 (1993) 126–128.
[23] H. Okamoto, Comment on Nd-Sn (neodymium-tin), J. Phase Equilibria. 15 (1994) 569–570. https://doi.org/10.1007/BF02649425.
[24] P. Riani, D. Mazzone, G. Zanicchi, R. Marazza, R. Ferro, F. Faudot, M. Harmelin, On the Ce-Cu-Sn System, J. Phase Equilib. 19 (1998) 239–251.
[25] H. Okamoto, Pr-Sn (Praseodymium-Tin), in: T.B. Massalski (Ed.), Bin. Alloy Phase Diagrams, 2nd ed., ASM International, Materials Park, Ohio, 1990.
[26] H. Okamoto, La-Sn (Lanthanum-Tin), J. Phase Equilibria. 23 (2002) 289.
[27] K. Huang, Y. Park, A. Ewh, B.H. Sencer, J.R. Kennedy, K.R. Coffey, Y.H. Sohn, Interdiffusion and reaction between uranium and iron, J. Nucl. Mater. 424 (2012) 82–88. https://doi.org/10.1016/j.jnucmat.2012.02.004.
[28] T. Chen, T.A. Smit, J.G. Gigas, D. Chen, R. Balerio, L. Shao, B. Sencer, J.R. Kennedy, Intermetallic formation and interdiffusion in diffusion couples made of uranium and single crystal iron, J. Nucl. Mater. 467 (2015) 82–88. https://doi.org/10.1016/j.jnucmat.2015.05.026.
[29] F.R. de Boer, R. Boom, W.C.M. Mattens, A.R. Miedema, A.K. Niessen, Cohesion in metals, transition metal alloys, North-Holland, Amsterdam, 1988.
[30] O. Kubaschewski, Review of alloy thermodynamics, Thermodyn. Nucl. Mater., Proc. Symp. (1968) 685–698.
[31] S. Chatain, C. Gueneau, D. Labroche, J. Rogez, O. Dugne, Thermodynamic assessment of the Fe-U binary system, J. Phase Equilibria. 24 (2003) 122–131. https://doi.org/10.1361/105497103770330730.
[32] Y.-C. Huang, W. Gierlotka, S.-W. Chen, Sn-Bi-Fe thermodynamic modeling and Sn-Bi/Fe interfacial reactions, Intermetallics. 18 (2010) 984–991. https://doi.org/10.1016/j.intermet.2010.01.026.
[33] A. Palenzona, S. Cirafici, Thermodynamic and crystallographic properties of REPd intermetallic compounds, Thermochim. Acta. 12 (1975) 267–275. https://doi.org/10.1016/0040-6031(75)85039-8.
[34] S.V. Meschel, O.J. Kleppa, Standard enthalpies of formation of some rare earth stannides by high temperature direct synthesis calorimetry, J. Alloys Compd. 238 (1996) 180–186. https://doi.org/10.1016/0925-8388(95)02190-6.